Materials Horizons

ROYAL SOCIETY OF CHEMISTRY

COMMUNICATION

View Article Online
View Journal

Published on 10 September 2021. Downloaded by Fudan University on 10/14/2021 1:32:05 PM.

Cite this: DOI: 10.1039/d1mh01287h

Received 13th August 2021,
Accepted 10th September 2021

DOI: 10.1039/d1mh01287h

rsc.li/materials-horizons

High performance polarization-sensitive self-powered imaging photodetectors based on a p-Te/n-$MoSe_2$ van der Waals heterojunction with strong interlayer transition†

Qixiao Zhao,[ab] Feng Gao,[c] Hongyu Chen, *[ab] Wei Gao,[ab] Mengjia Xia,[ab] Yuan Pan,[ab] Hongyan Shi,[d] Shichen Su, [abe] Xiaosheng Fang *[f] and Jingbo Li*[ab]

In-plane anisotropic two-dimensional (2D) materials offer great opportunities for developing novel polarization sensitive photodetectors without being in conjunction with filters and polarizers. However, owing to low linear dichroism ratio and insufficient optical absorption of the few layer 2D materials, the comprehensive performance of the present polarization sensitive photodetectors based on 2D materials is still lower than the practical application requirements. In this work, after systematic investigation of the structural, vibrational, and optical anisotropies of layer-structured Te nanosheets, a novel polarization-sensitive self-powered imaging photodetector with high comprehensive performance based on a p-Te/n-$MoSe_2$ van der Waals heterojunction (vdWH) with strong interlayer transition is proposed. Owing to the high rectification ratio (10^4) of the diode, the device shows excellent photovoltaic characteristics. As examples, the photodetectors exhibited an ultra-high on/off ratio of 10^5 at a relatively weak light intensity (4.73 mw cm^{-2}), and the highest responsivity of the device could reach 2106 mA W^{-1} without any power supply. In particular, benefitting from the excellent dichroism properties of Te nanosheets synthesized in this work, the anisotropic ratio of the photocurrent (I_{max}/I_{min}) could reach as high as 16.39 (405 nm, 24.2 mw cm^{-2}). This value obtained under zero bias voltage is much greater than that of present 2D material photodetectors even at a bias voltage. In addition, the highest detectivity is 2.91×10^{13} Jones at a low bias voltage of -0.08 V. This work provides a novel building block for high resolution polarization-sensitive photodetection of weak signals in complex environments.

New concepts

In order to precisely identify the targets in several concealed, camouflaged, and non-cooperative backgrounds, extensive efforts have been carried out to explore the schemes of polarization-sensitive photodetectors with a small volume. Benefiting from the intrinsically in-plane anisotropic crystal structures, several 2D semiconductors were explored for constructing monolithic polarization-sensitive photodetectors. However, due to the low absorption, insufficient polarization sensitivity, and lack of air stability, the comprehensive performance of these devices based on 2D semiconductors is still lower than required for practical applications. Herein, a novel polarization-sensitive self-powered imaging photodetector with high comprehensive performance based on a p-Te/n-$MoSe_2$ vdWH is proposed. In particular, owing to the excellent dichroism properties of Te nanosheets synthesized in this work and strong interlayer transition of the p-Te/n-$MoSe_2$ vdWH, the anisotropic ratio of photocurrent could reach as high as 16.39 without any power supply. This value is 7 times larger than that of present Te-based photodetectors. It is believed that the p-Te/n-$MoSe_2$ vdWHs would provide additional opportunity for constructing a compact monolithic polarization-sensitive imaging system with low energy consumption.

Introduction

Driven by the rapid development of information technology (IT), photodetectors with the unique ability of converting optical signals into electrical signals have stretched throughout every facet of our lives.[1] In particular, imaging photodetectors operated at different wavelengths are essential for many domains including flame detection, converting communication, medical diagnosis, night vision, and remote sensing, *etc.*[2–4] However, as conventional photodetectors can only provide spectral information and the corresponding intensity of

[a] Institute of Semiconductor Science and Technology, South China Normal University, Guangzhou 510631, P. R. China. E-mail: chenhy@m.scnu.edu.cn, jbli@m.scnu.edu.cn
[b] Guangdong Province Key Lab of Chip and Integration Technology, Guangzhou 510631, P. R. China
[c] Key Laboratory of Micro-systems and Micro-structures Manufacturing of Ministry of Education, Harbin Institute of Technology, Harbin 150080, P. R. China
[d] Department of Physics, Harbin Institute of Technology, Harbin 150080, P. R. China
[e] SCNU Qingyuan Institute of Science and Technology Innovation Co., Ltd, Qingyuan 511517, P. R. China
[f] Department of Materials Science, Fudan University, Shanghai 200433, P. R. China. E-mail: xshfang@fudan.edu.cn

† Electronic supplementary information (ESI) available. See DOI: 10.1039/d1mh01287h

Published on 10 September 2021. Downloaded by Fudan University on 10/14/2021 1:32:05 PM.

optical radiations, it is difficult for them to precisely identify the targets in several concealed, camouflaged, and non-cooperative backgrounds. Inspired by the polarization-sensitive photoreceptors of several animals such as cuttlefish,[5] a kind of special functional photodetector with the ability of obtaining polarization imaging exhibits low false alarm in conjunction with the reflection, scattering, and transmission information of the object in a complex environment. Simply, the core of polarization-sensitive photodetection technology is constructing devices with the conformation and orientation of the material/device structures.[6]

Until now, most technological implementations of polarization-sensitive photodetection are realized by nonmonolithic approaches, in which polarizers are positioned in front of the photodetectors. Under the impetus of rapidly developing nanotechnology, the ability of shrinking the size of the photodetectors and manipulating light with certain vibration at a small volume is essential. And extensive efforts have been carried out for exploring the schemes of monolithic polarization-sensitive photodetectors. Although orientating in anisotropic device patterns such as quantum-well structures,[7] and one-dimensional (1D) nanostructures including InP,[8] ZnO,[9] and CdS[10] nanowires (NWs) and so forth are proposed as potential building blocks for constructing polarization-sensitive photodetectors, these demand sophisticated patterning and aligning processes. Additionally, the randomness and aspect ratios of 1D materials would limit the diversified device preparation.[11,12]

In contrast, benefiting from the intrinsically in-plane anisotropic crystal structures, the emerging two-dimensional (2D) layered semiconductors such as black phosphorus (BP), antimonene, ReS_2, $ReSe_2$, GeAs, GeSe, and $GeSe_2$, *etc.* have been extensively explored by our[13–17] and other groups[18–21] as the active materials of monolithic polarization-sensitive photodetectors. However, due to the low absorption, insufficient polarization sensitivity, and lack of air stability, the comprehensive performance of these kinds of polarization-sensitive photodetectors is still lower than practical applications. Additionally, some polarization-sensitive photodetectors are needed for long-term working in some unmanned hazardous atmospheres or harsh environments. Until now, high performance self-powered polarization-sensitive photodetector materials operating without any power supply are still lacking.

Nowadays, great efforts in fabricating self-powered photodetectors have been demonstrated in our[22–26] and other previous studies[27–30] through the construction of p–n junctions, Schottky junctions, and heterojunctions by the photovoltaic effect. Due to the nature of dangling bond-free surfaces enabling 2D layered materials to integrate other desirable materials into vdWH without consideration of the crystal lattice mismatch, it would be greatly advantageous to explore novel vdWH configurations of polarization-sensitive self-powered photodetectors by a facile and low-cost approach.

Fortunately, as a quasi 2D layered semiconductor, Tellurium (Te) is a rising star building block for polarization-sensitive photodetection owing to several excellent unique properties such as high carrier mobility of $\sim 10^3$ cm^2 $(V*S)^{-1}$, adjustable bandgap (0.35–1.2 eV), high linear dichroism, and outstanding environmental stability at room temperature.[31,32] Therefore, to further enhance the photoelectric conversion efficiency and the polarization-sensitivity of the present Te based polarization-sensitive photodetectors, the structural, vibrational, and optical anisotropies of layer-structured Te nanosheets synthesized by a solution synthesized method are systematically investigated, and then multilayer $MoSe_2$ nanosheets with stronger optical absorbance (Absorbed Photon Flux J_{abs} $\sim$4.6 mA cm^{-2}),[33] broad spectral selectivity (400–900 nm),[34] stability, and high carrier mobility (50–100 cm^2 V^{-1} s^{-1})[35] are selected to construct high-performance p-Te/n-$MoSe_2$ vdWHs with a strong interfacial coupling effect by facile exfoliation and transfer technologies for fabricating a self-powered polarization-sensitive photodetector. Owing to the high rejection ratio (10^4) of the diode, the as-assembled p-Te/n-$MoSe_2$ vdWH exhibits excellent photovoltaic behavior. As examples, the device could achieve a large on/off ratio of 10^5, high responsivity of 2106 mA W^{-1}, and high external quantum efficiency (EQE) of 645% without any power supply at the wavelength of 405 nm. More importantly, owing to the highly anisotropic optical properties of Te nanosheets, the self-powered photodetectors exhibit a strong polarization-sensitive photocurrent up to 16.39 at 405 nm. To the best of our knowledge, the photocurrent anisotropy ratio of p-Te/n-$MoSe_2$ vdWH is 7 times more than that of Te-based photodetectors.[32,36] In addition, due to the high detectivity of the device (2.91×10^{13} Jones) at a small bias voltage (−0.08 V), this photodetector can not only realize high-resolution imaging, but also distinguish the polarization of incident light effectively.

Results and discussion

To construct the polarization sensitive photodetector based on p-Te/n-$MoSe_2$ vdWH, highly crystalline Te nanosheets were synthesized *via* a facile solution-grown process at first (Fig. S1, ESI†). Fig. 1a is the optical image of the as-fabricated nanosheets with a relatively smooth surface. It can be found that the length of the nanosheets ranges from 40 to 90 μm, and the width of the nanosheets ranges from 3 to 11 μm. Subsequently, the mophology, chemical composition, and crystal structure of these nanosheets is further confirmed by transmission electron microscopy (TEM) and energy dispersive X-ray spectroscopy (EDS). Fig. S2 (ESI†) demonstrates that a Te element is homogeneously distributed throughout the nanosheets in the EDS mapping image. Fig. 1b is the high-resolution TEM (HRTEM) image and corresponding selected-area electron diffraction (SAED) pattern. The bright and clear diffraction spots exhibited that the as-fabricated Te nanosheets have a helical chain structure along the [0001] direction. The lattice constant along the [0001] direction is 5.97 nm, the *d*-spacing of the {1210} plane family is 2.19 Å, the *d*-spacing of the {0001} plane family is 5.97 Å, and the angle between the (0001) and $(1\bar{2}10)$ crystallographic planes is 90°. The crystal structure of Te is shown in Fig. S3 (ESI†). The helical chains along the [0001] direction are defined as the *c*-axis of the crystal.

 This journal is © The Royal Society of Chemistry 2021

Published on 10 September 2021. Downloaded by Fudan University on 10/14/2021 1:32:05 PM.

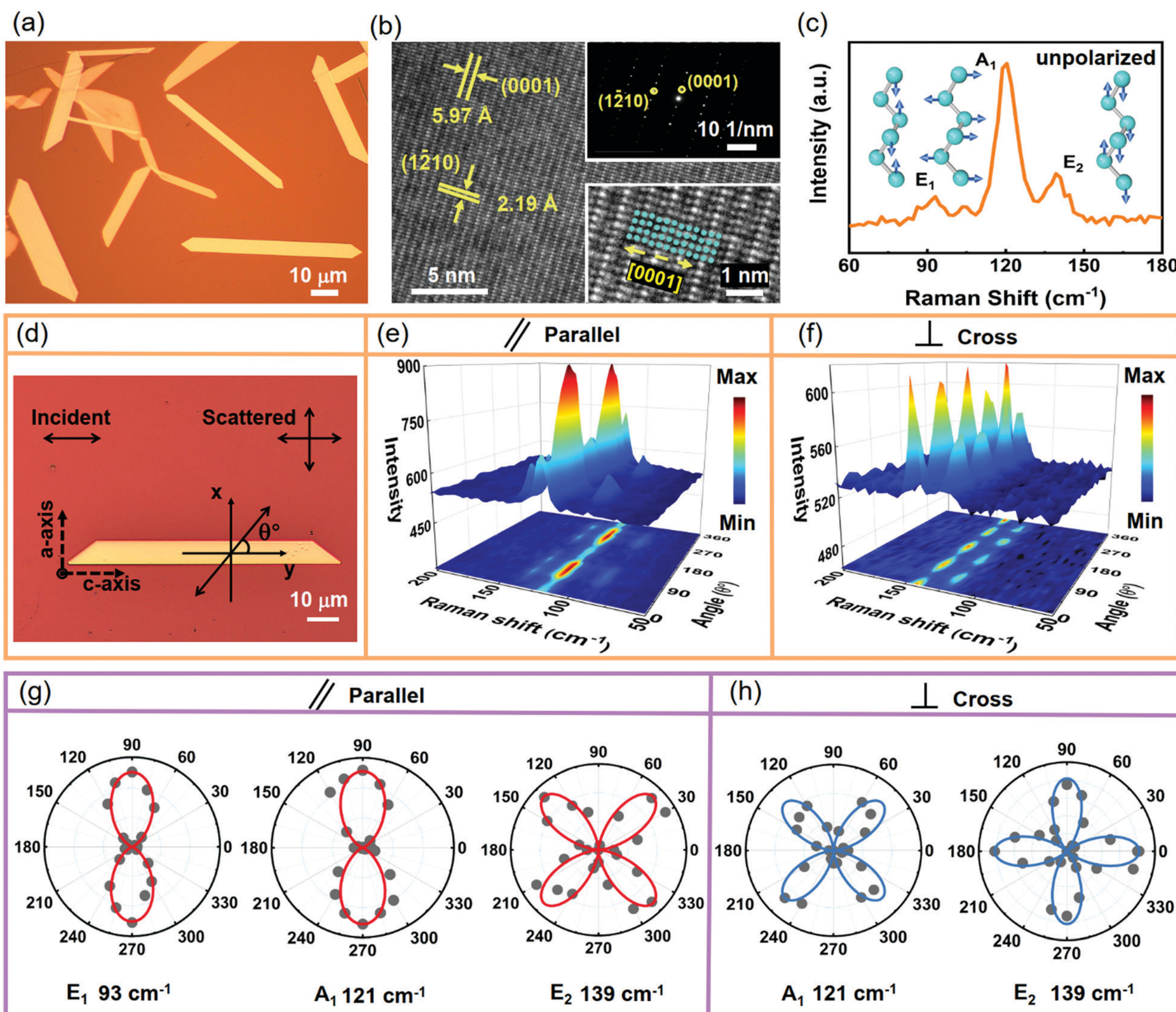

Fig. 1 Material characterization and anisotropic characterization of solution-grown Te nanosheets. (a) Optical microscope image of Te nanosheets. (b) HRTEM image taken from a Te nanosheet. Inset: Diffraction pattern of a Te nanosheet. (c) Atomic vibrational patterns of E_1, A_1, and E_2 phonon modes in Te Raman spectra and their corresponding atom vibration directions. (d) Optical microscope (OM) image of the measured nanosheet, showing the crystallographic axes, the experimental coordinates, and the directions of the incident and analyzed scattered light, and indicating the angle θ between the incident light and the y direction (c-axis). (e) Polarized Raman intensity mapping of Te nanosheets as a function of wave number and incident angle in parallel-polarized configurations. (f) Polarized Raman intensity mapping of Te nanosheets as a function of wave number and incident angle in cross-polarized configurations. (g) Polar plot of E_1, A_1 and E_2 mode intensity in parallel-polarized configurations. (h) Polar plot of A_1 and E_2 mode intensity in cross-polarized configurations.

It means that the nanosheets fabricated in this work are formed from high-quality γ-Te single crystals with *c*-axis preferred orientation.[37–39] Therefore, the as-fabricated multilayer nanosheets are confirmed to be pure γ-Te with an asymmetric point group of D_3.[40] To further evaluate the phonon vibration and crystal orientation of the fabricated Te nanosheets, Raman measurements are implemented.[41] The Raman spectrum shown in Fig. 1c exhibits three peaks located at 93 cm^{-1}, 121 cm^{-1}, and 139 cm^{-1}, which are in good agreement with the E_1, A_1, and E_2 phonon modes of Te. In detail, the aforementioned three phonon modes of Te correspond to the bending of the bond rotating around the *a*-axis, the chain expansion mode of each atom moving on the base plane, and the asymmetric stretching of the helical chain along the *c*-axis, respectively.[42] The identification of the *a*-axes and *c*-axes of our sample, shown in Fig. 1d, was carried out by angle-resolved polarized Raman spectroscopies (ARPRSs) as measured directly. In Fig. 1d, the *c*-axis is defined as the *y* direction in the experimental coordinate, the *x* direction is perpendicular to the *a*-axis, and θ is the angle between the directions of the *c*-axis and the incident light. It can be found that in Fig. 1e and f, the different Raman mode intensities change periodically with the variation of rotation angle under the parallel-, and cross-polarized configurations, indicating a strong in-plane vibration anisotropy. Under a parallel polarization configuration (Fig. 1e), A_1, E_1 photon mode exhibits a period of π, and the E_2 mode exhibits a

Published on 10 September 2021. Downloaded by Fudan University on 10/14/2021 1:32:05 PM.

period of π/2, while under the cross polarization configuration, all modes exhibit a period of π/2 (Fig. 1f). In contrast, under the cross configuration, the intensity tendency of the E_1 mode is not observed due to its low intensity value. In order to reveal the dependence of the angle-resolved Raman and crystal axis orientation more intuitively, the peak intensities of different modes are extracted and plotted into corresponding polar graphs (Fig. 1g and h). The polarized Raman intensity is fitted through Raman tensor analysis,[43] and the Raman scatter intensity (*I*) of the peak can be expressed as

$$I \propto |e_i R\, e_s|^2 \tag{1}$$

where *R* is the Raman tensor, and e_i and e_s are the electric field vectors of the incident and scattered light, respectively. Under the parallel configuration,

$$e_i = [\sin\theta\; 0\; \cos\theta] \tag{2}$$

$$e_s = [\sin\theta\; 0\; \cos\theta] \tag{3}$$

while for the cross configuration,

$$e_i = [\sin\theta\; 0\; \cos\theta] \tag{4}$$

$$e_s = \left[\sin\left(\theta+\frac{\pi}{2}\right) 0 \cos\left(\theta+\frac{\pi}{2}\right)\right]^T = [\cos\theta 0 - \sin\theta]^T \tag{5}$$

where variable θ is the angle between the *c*-axis of the crystal and the polarization direction of the incident light. The ultrathin trigonal Te belongs to the D_3 point group. The Raman tensors of A_1, E_1 and E_2 modes are given as follows:[40]

$$R(A_1) = \begin{bmatrix} a & 0 & 0 \\ 0 & a & 0 \\ 0 & 0 & b \end{bmatrix} \tag{6}$$

$$R(E_1) = \begin{bmatrix} c & 0 & 0 \\ 0 & -c & d \\ 0 & d & 0 \end{bmatrix} \tag{7}$$

$$R(E_2) = \begin{bmatrix} 0 & -c & -d \\ -c & 0 & 0 \\ -d & 0 & 0 \end{bmatrix} \tag{8}$$

where *a*, *b*, *c*, and *d*, are Raman tensor elements. The polarized Raman intensity *I* for the different modes can be obtained as follows:

$$I(A_1)^{\parallel} = |a\sin^2\theta + b\cos^2\theta|^2 \tag{9}$$

$$I(E_1)^{\parallel} = |c\sin^2\theta|^2 \tag{10}$$

$$I(E_2)^{\parallel} = |2c\sin\theta\;\cos\theta|^2 \tag{11}$$

$$I(A_1)^{\perp} = \left|\frac{a-b}{2}\sin 2\theta\right|^2 \tag{12}$$

$$I(E_1)^{\perp} = \left|\frac{c}{2}\sin 2\theta\right|^2 \tag{13}$$

$$I(E_2)^{\perp} = |-d\cos 2\theta|^2 \tag{14}$$

where ∥ and ⊥ represent the parallel and cross-polarization configurations, respectively. As shown in Fig. 1g and h, Raman spectra agree very well with the theoretical prediction. In addition, based on the Raman tensor analysis, the *a*-axis direction of the crystal orientation can be determined by the intensity of the E_1 mode, the direction of the maximum intensity of the E_1 peak.[36] The ARPRS show that the *c*-axis of the selected 2D Te is consistent with the orientation of the *y* direction of the nanosheet, which corroborates our TEM analysis.

In order to confirm that the p-Te/n-$MoSe_2$ vdWH has been formed, SEM images and associated element mapping of p-Te/n-$MoSe_2$ vdWH are characterized (Fig. 2a and b). The SEM image and corresponding element mapping demonstrates that the p-Te/n-$MoSe_2$ vdWH device is uniformly fabricated on the SiO_2/Si substrate with a relatively smooth surface. The energy-dispersive X-ray spectroscopy (EDS) analysis in Fig. 2b further affirms that the chemical composition of the obtained p-Te/n-$MoSe_2$ vdWH consisted of Mo, Se and Te elements, and the Mo/Se ratio of the $MoSe_2$ sample is close to 1 : 2. The thickness of the $MoSe_2$ and Te nanosheets is 24.55 nm and 27.94 nm by AFM (Fig. S5, ESI†). Raman mapping of p-Te/n-$MoSe_2$ vdWH (Fig. S6, ESI†) with the homogeneity of each component of Te, $MoSe_2$ and Te/$MoSe_2$, and the three peaks in the Raman spectra collected near the red dots, yellow dots and blue dots in Fig. 2c exhibit no obvious shift, demonstrating the good quality of the p-Te/n-$MoSe_2$ vdWH after the mechanical exfoliation, and target-transfer processes.[44] The SAED pattern of the heterojunction region shows two sets of clearly distinguishable diffraction patterns of different orientations (Fig. 2d), which proves that the high-quality of the p-Te/n-$MoSe_2$ vdWH is fabricated as shown in Fig. S7 (ESI†).

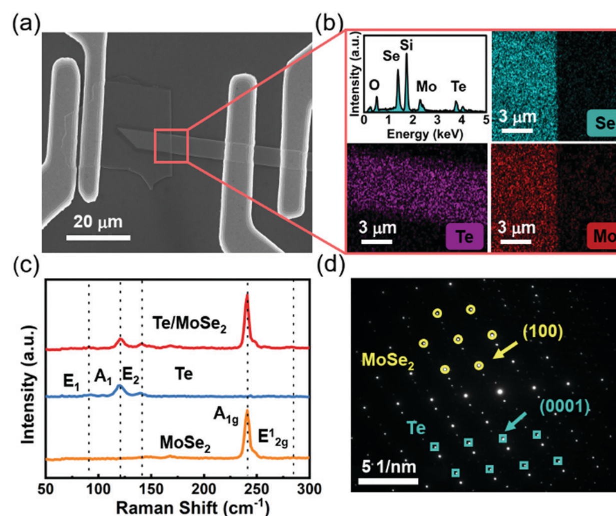

Fig. 2 Polarization-sensitive self-powered photodetector based on a p-Te/n-$MoSe_2$ van der Waals heterojunction. (a) SEM images p-Te/n-$MoSe_2$ van der Waals heterojunction device. (b) Elemental mapping images and the corresponding EDS. (c) Raman spectra of Te, $MoSe_2$, and the overlapped region in the heterojunction device. (d) The SAED pattern collected near the overlapped region in the heterojunction shows two sets of oriented electron diffraction patterns, corresponding to Te and $MoSe_2$.

This journal is © The Royal Society of Chemistry 2021

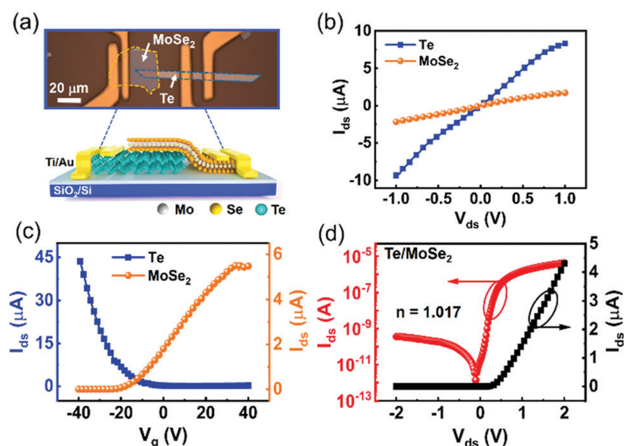

Fig. 3 Electronic characteristics of p-Te/n-$MoSe_2$ vdWH. (a) Schematic illustration of the p-Te/n-$MoSe_2$ vdWH device. Inset: OM image of the p-Te/n-$MoSe_2$ vdWH device. (b) I_{ds}–V_{ds} curves of Te and $MoSe_2$ at V_g = 0 V. (c) The transfer curves of the Te and $MoSe_2$ field-effect transistors. (d) I_{ds}–V_{ds} curves of the p-Te/n-$MoSe_2$ vdWH device at V_g = 0 V.

To study the electric properties of the aforementioned Te/$MoSe_2$ vdWH, *I*–*V* characteristic measurements of the diode were first carried out under dark conditions. Fig. 3a is the optical image of the device (top view). To demonstrate the structure of the device vividly, a side view of the structural models is shown in the inset of Fig. 3a. The linear characteristic of the I_{ds}–V_{ds} curves in Fig. 3b indicates the ideal Ohmic contact of both the Ti–$MoSe_2$–Ti and Ti–Te–Ti devices. And the transfer curves of the Te and $MoSe_2$ field-effect transistors obtained in Fig. 3c demonstrated that Te is a p-type material and $MoSe_2$ is a n-type material in this work. I_{ds}–V_{ds} curves in Fig. 3d exhibit a significant rectification behavior of p-Te/n-$MoSe_2$ vdWH with the ideality factor (n) of 1.017, which is very close to the ideal p–n junction diode (n = 1).[45] In particular, the p-Te/n-$MoSe_2$ vdWH device with a high rectification factor of 10^4 at ±2 V still exhibits a very low dark current of 363 pA even under a bias voltage of −2 V. This value of dark current is smaller than that of the pristine Te, $MoSe_2$ device (mA) and the rectification factor is larger than that of Te-based and $MoSe_2$-based photodetectors reported at present.[26,46,47] Therefore, the significant rectification characteristic of the p-Te/n-$MoSe_2$ vdWH diode in this work is mainly originated from the Te–$MoSe_2$ p–n junctions instead of metal-semiconductor contact.

To examine the self-powered character of this diode, *I*–*t* curves of p-Te/n-$MoSe_2$ vdWH were measured under the illumination wavelengths of 405 nm, 532 nm, 635 nm and 808 nm at 0 V. As shown in Fig. 4a, photocurrents of the p-Te/n-$MoSe_2$ vdWH photodiodes could change immediately with highly repeatable photoswitching characteristics and better stability when the light switched between on and off. Particularly at the wavelength of 405 nm, the device exhibits an ultra-low dark current of 10^{-14} A and a significant photocurrent of 10^{-8} A (Fig. S8, ESI†). This means that the photoresponse on/off ratio could reach up to 5 orders of magnitude. In addition, the photocurrent is steadily increasing with increasing the power density of incident light (405 nm). It demonstrated that the number of photogenerated carriers is proportional to the absorbed luminous flux. Based on the ultra-high photoresponse on/off ratio of the photodetectors, linear dynamic range properties (LDR) are further analyzed at zero bias voltage. Generally, the LDR can characterize the light intensity range of the photodetectors with constant responsivity, which can be given by[48]

$$\mathrm{LDR} = 20\log\left(\frac{I_{\mathrm{ph}}}{I_{\mathrm{d}}}\right) \tag{15}$$

$$I_{\mathrm{ph}} = I_{\mathrm{illumination}} - I_{\mathrm{dark}} \tag{16}$$

where I_{ph} is the photocurrent, $I_{illumination}$ is the illumination current, and I_d is the dark current. The calculated LDR can exceed 110 dB (Fig. 4b), which is superior to the InGaAs-based photodetector (66 dB).[49,50] In addition, the device exhibited a significant photovoltaic characteristic as well. As examples, the maximum open-circuit voltage (V_{OC}) and the maximum short-circuit current (I_{SC}) could reach up to 0.25 V and 72 nA when the light intensity increases to 42.8 mW cm^{-2} (Fig. 4c). And the maximum output electrical power could reach 5.76 nw at 405 nm (42.8 mW cm^{-2}) (Fig. S9, ESI†).

In order to further confirm the performance of the self-powered photodetector, detailed data on the responsivity (R) and external quantum efficiency (EQE) were investigated at 0 V using a 405 nm laser with the power density ranging from 0.04 to 42.8 mW cm^{-2} as the light source. Responsivity and EQE of the p-Te/n-$MoSe_2$ vdWH photodetector can be determined by:

$$R = \frac{I_{\mathrm{ph}}}{P} \tag{17}$$

$$\mathrm{EQE} = \frac{hcR}{e\lambda} \tag{18}$$

where I_{ph} is the photocurrent, P is the incident light power, λ is the wavelength of incident light, e is the electronic charge, h is the Planck constant, and c is the light velocity. It can be found in Fig. 4d that the highest responsivity and EQE values could reach 2.1 A W^{-1} and 645%, respectively, which is better than commercial Si photodetectors (≤1 A W^{-1}).[51] In addition, both the responsivity and EQE decreased slightly with increasing light power intensity. This phenomenon may originate from the self-heating-induced increase in the charge carrier scattering and the rate of charge recombination.[52]

The detectivity (D^*) is one of the key Fig.-of-merits for a photodetector, which usually describes the smallest detectable signal. D^* is defined as:

$$D^* = \frac{RS^{\frac{1}{2}}}{(2eI_{\mathrm{d}})^{\frac{1}{2}}} \tag{19}$$

where R is the responsivity, S is active area, e is the electronic charge, and I_d is the dark current. The calculated detectivity of

Published on 10 September 2021. Downloaded by Fudan University on 10/14/2021 1:32:05 PM.

Published on 10 September 2021. Downloaded by Fudan University on 10/14/2021 1:32:05 PM.

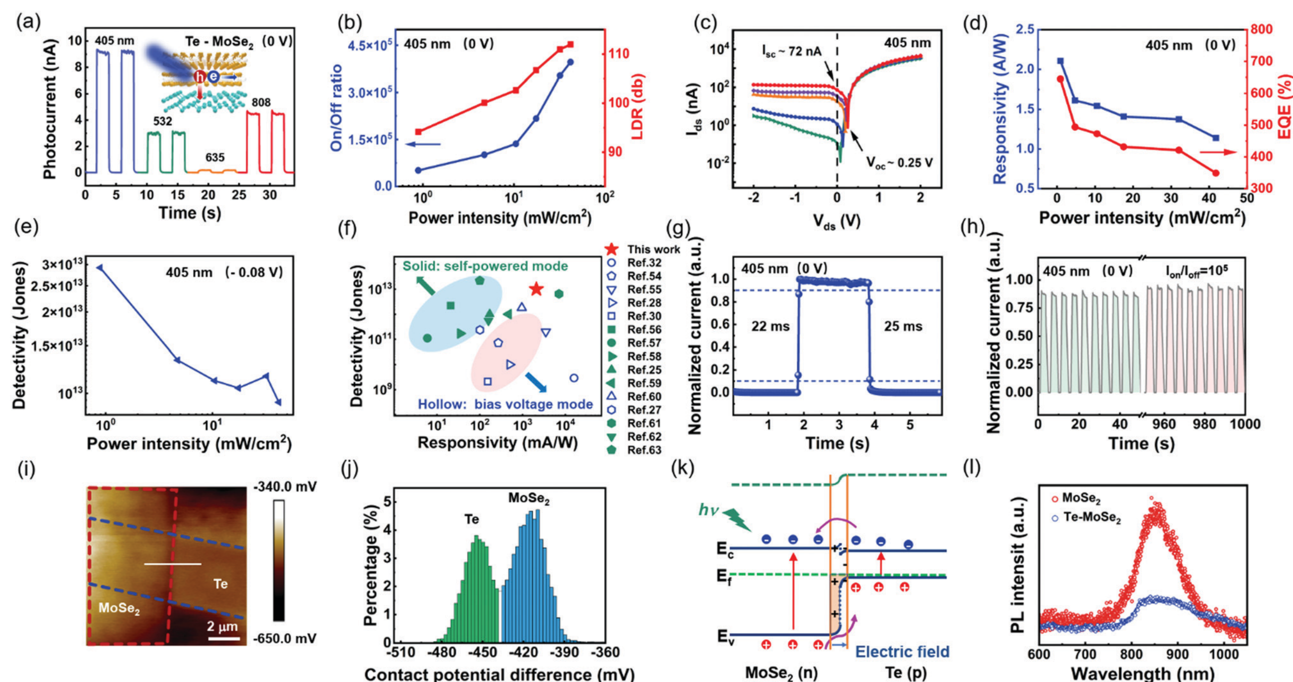

Fig. 4 Self-driven photoresponse characteristics of p-Te/n-$MoSe_2$ vdWH. (a) Photoresponse of the heterostructure under different light wavelengths (405, 532, 635 and 808 nm, 10 mW cm^{-2}) at zero bias voltage. Inset: Schematic diagram of the separation process of photogenerated carriers on the interface of p-Te/n-$MoSe_2$ vdWH under laser illumination. (b) Photoresponse on/off ratio and linear dynamic range (LDR) of p-Te/n-$MoSe_2$ vdWH under varied power intensities at zero bias voltage. (c) I_{ds}–V_{ds} measurements under different laser power intensity of 405 nm for p-Te/n-$MoSe_2$ vdWH. (d) Responsivity (R) and External Quantum Efficiency (EQE) of p-Te/n-$MoSe_2$ vdWH under varied power intensities at zero bias voltage. (e) Detectivity (D^*) of the p-Te/n-$MoSe_2$ vdWH device. (f) Performance summary of self-powered photodetectors based on 2D semiconductors. (g) One cycle of the photoresponse to a wavelength of 405 nm at zero bias voltage for estimating both the rise and fall time. (h) Time-dependent photoresponse under 200 on/ooff switching cycles. (i) KPFM mapping images of the Te/$MoSe_2$ vdWH. (j) Histogram distributions of VCPD extracted from the KPFM mapping image. (k) Energy band diagram and carrier transport of the Te and $MoSe_2$ for after contact and under light irradiation at 0 V. (l) PL spectra of the $MoSe_2$ and p-Te/n-$MoSe_2$ vdWH.

devices is plotted in Fig. 4e. And the detectivity of the device is as high as 2.91×10^{13} Jones at the wavelength of 405 nm (0.89 mW cm^{-2}). The performance comparison between our p-Te/n-$MoSe_2$ vdWH photodetector and other 2D photodetectors reported previously is shown in Fig. 4f. Our p-Te/n-$MoSe_2$ vdWH photodetector has a remarkable advantage compared to other 2D photodetectors.[25,27,28,30,32,53–62] On the other hand, the photoresponse of our self-powered device was very fast, highly stable and reproducible. As shown in Fig. 4g, the 10–90% response time and decay time were measured to be 25 ms and 22 ms, respectively. And the excellent repeatable photoresponse after 200 switching cycles indicates a high reliability of our device (Fig. 4h).

To explore the working mechanisms of the high photoresponse characteristics for the p-Te/n-$MoSe_2$ vdWH photodiodes, Kelvin Probe Force Microscopy (KPFM) is employed to unveil the trend of Fermi level shift of Te and $MoSe_2$, as well as the band alignment in p-Te/n-$MoSe_2$ vdWH (Fig. 4i–k). The contact potential difference (V_{CPD}) between the probe tip and the sample is given by

$$V_{CPD} = \frac{W_{Tip} - W_{Sample}}{e} \tag{20}$$

where W_{tip} and W_{sample} are the work function of the tip and the sample, and e is the elementary charge, respectively. Therefore, the work function difference of the nanosheets can be calculated by measuring the V_{CPD} difference. As shown in Fig. 4j, the V_{CPD} difference of the Te/$MoSe_2$ vdWH is determined to be about 40.08 mV. Based on the KPFM result, the energy band diagrams are proposed in Fig. S10 (ESI†). Due to the difference of Fermi level (EF), the electrons would diffuse from $MoSe_2$ into Te while holes should diffuse from Te into $MoSe_2$ when p-type Te comes into contact with n-type $MoSe_2$. Therefore, the energy level near the Te surface bends upward, while the energy level near the $MoSe_2$ surface bends downwards. Eventually, the Fermi levels of Te and $MoSe_2$ are arranged at the same level, resulting in the formation of a built-in electric field near the p-Te/n-$MoSe_2$ interface (Fig. 4k). Moreover, a strong built-in electric field and a depletion layer formed near the junction region are capable of reducing the electron–hole recombination and preventing the electron transport from $MoSe_2$ to Te, favoring a low reverse dark current and thus improving the detectivity. To confirm the above statement of carrier transfer at the p-Te/n-$MoSe_2$ interface, photoluminescence (PL) spectra of $MoSe_2$ and the p-Te/n-$MoSe_2$ vdWH were measured as well. As shown in Fig. 4l, the significant quenching of the PL intensity in p-Te/n-$MoSe_2$ vdWH indicates the transfer of photogenerated carriers between Te and $MoSe_2$, leading to an increase in the increase of non-radiative recombination and the

This journal is © The Royal Society of Chemistry 2021

Published on 10 September 2021. Downloaded by Fudan University on 10/14/2021 1:32:05 PM.

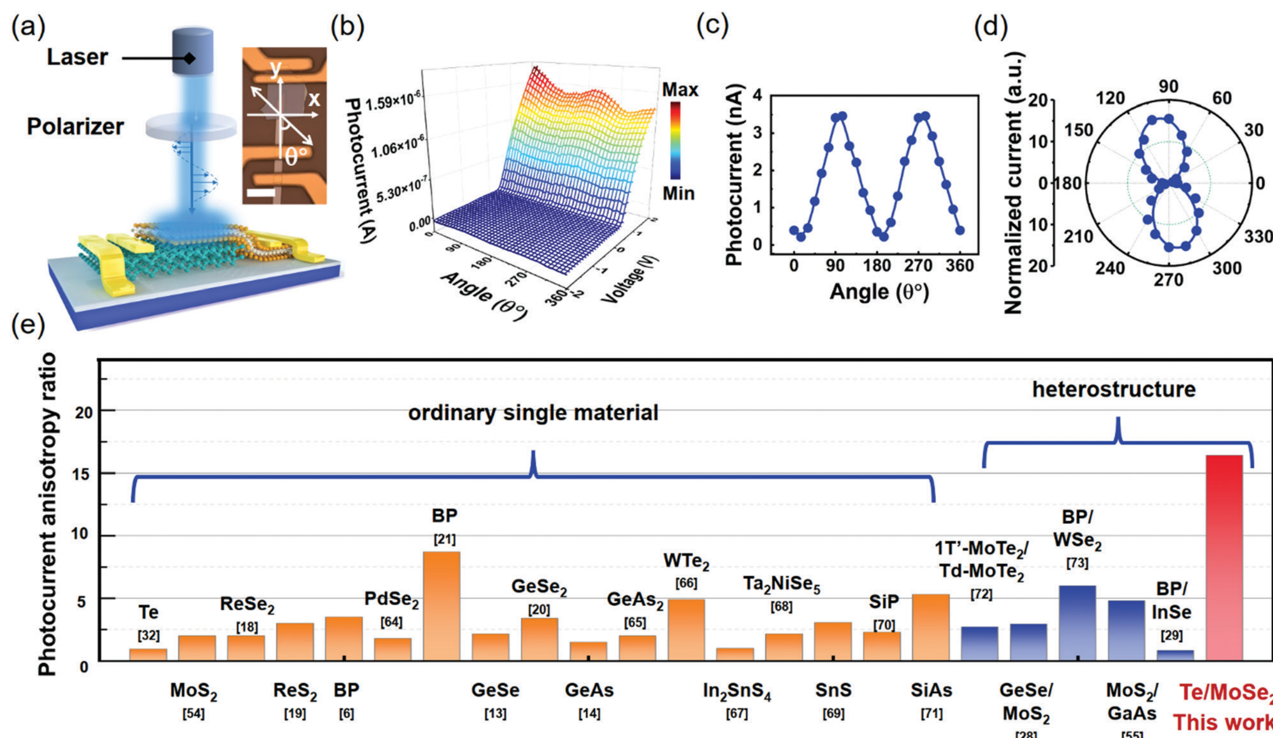

Fig. 5 Polarization-sensitive photodetection of the p-Te/n-$MoSe_2$ vdWH. (a) Schematic diagram of the experimental setup for polarization-resolved photocurrent measurement. θ is the angle between the polarization direction of incident light and the *y* direction (*c*-axis of Te nanosheets). The scale bar is 20 mm. (b) The polarized photocurrent for the wavelengths of 405 nm at room temperature, under the light power intensity of 24.2 mW cm^{-2}. (c) Polarized photocurrent for the incident wavelengths of 405 nm (24.2 mW cm^{-2}) at zero bias voltage. (d) Polar diagram of the polarized photocurrent for the incident wavelengths of 405 nm at zero bias voltage, and the anisotropic ratio of 16.39. (e) Photocurrent anisotropy ratio comparison for various 2D materials.

decrease of PL emission recombination. Therefore, KPFM and PL results clearly indicate a strong interfacial coupling in p-Te/n-$MoSe_2$ vdWH.[63]

As mentioned above, strong intrinsic anisotropy of Te nanosheets and excellent photovoltaic properties of the p-Te/n-$MoSe_2$ vdWH photodetector offer us additional opportunities to further explore the polarization sensitive photoresponse of the device. In view of this, polarization-resolved photocurrents of the p-Te/n-$MoSe_2$ vdWH self-powered photodetector were measured with a laser (405 nm, 12.2 mW) as the optical source, and the measurement setup is shown in Fig. 5a. And then the polarization-dependent photocurrent of the device from −2.0 V to 2.0 V at 405 nm is obtained. θ is the angle between the polarization direction of incident light and the *c*-axis of Te nanosheets. It can be found that in Fig. 5b, the measured photocurrent depends on the polarization angle and bias voltage. To better illustrate the self-powered performance of the polarized photodetector, Fig. 5c exhibits the polarization-resolved photocurrents of the device at zero bias voltage. It is obvious that the photocurrent changes periodically when the θ is rotated from 0° to 360°. The photocurrent reaches the maximum when the value of θ is 90° and 270°, respectively. This direction is corresponding well to the *a*-axis direction of Te nanosheets. On the other hand, the minimum value of the photocurrent is exhibited at 0° and 180°, which is corresponding to the *c*-axis direction of Te nanosheets. In addition, ARPRSs tests, polarized photodetection and in-plane electrical transport characteristics of the $MoSe_2$ device were performed and the results revealed that $MoSe_2$ is in-plane isotropic (Fig. S13, ESI†). Therefore, the anisotropic photocurrent observed in this work is originated from the Te layer instead of the $MoSe_2$ layer. In order to observe the polarized photoresponse more intuitively, a polar diagram of the normalized polarized photocurrent for the incident wavelengths of 405 nm at zero bias voltage is exhibited (Fig. 5d). The points were fitted by the function:

$$I_{ph}(\theta) = I_{phmax}\cos^2(\theta + \varphi) + I_{phmin}\sin^2(\theta + \varphi) \quad (21)$$

where the I_{phmax} and I_{phmin} represent the maximum and minimum photocurrent, θ is the polarization angle and ϕ is the fitting parameter. According to the experimental data in Fig. 5d, the calculated photocurrent anisotropy ratio (I_{phmax}/I_{phmin}) could reach as large as ~16.39. In addition, to further confirm the polarized photoresponse of the p-Te/n-$MoSe_2$ vdWH device, the polarized photocurrent is also studied under the irradiation of a laser with 635 nm wavelength (Fig. S14, ESI†). The calculated photocurrent anisotropy ratio is also as high as ~13.97. Meanwhile, two other heterojunction devices were also checked, and the photocurrent anisotropy ratio shows a good consistency (Fig. S15, ESI†). It is noteworthy that the

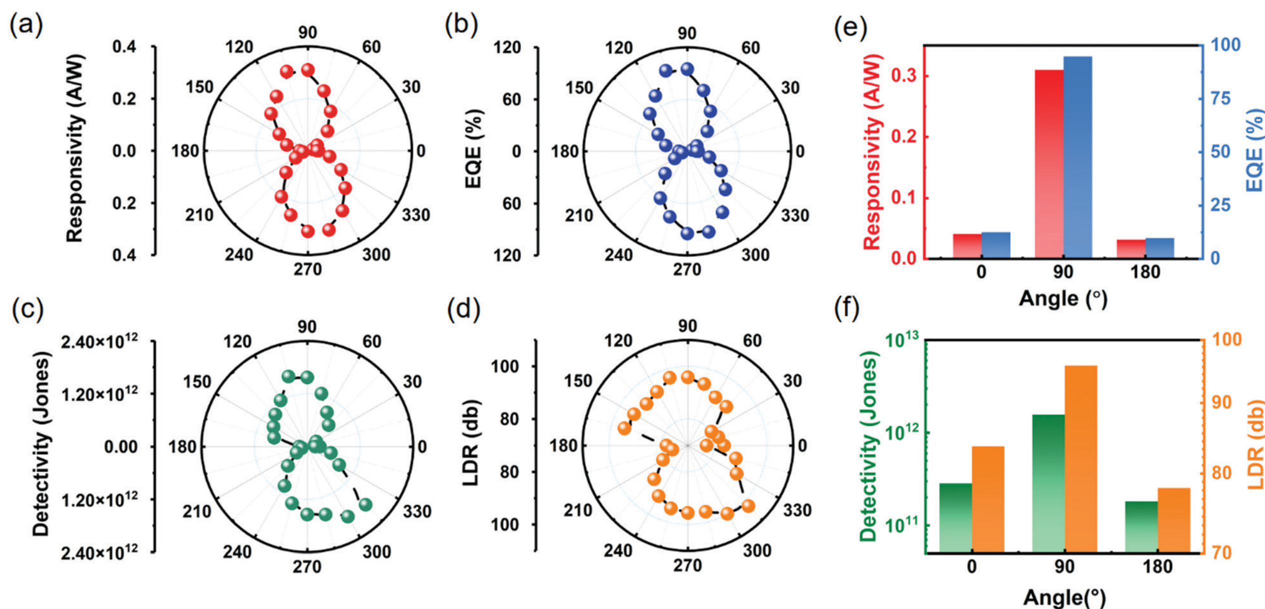

Fig. 6 Polarization-sensitive photodetection of p-Te/n-$MoSe_2$ vdWH. (a–d) Polar diagram of the polarized responsivity (a), EQE (b), detectivity (c), and LDR (d) for the incident wavelengths of 405 nm (24.2 mW cm^{-2}) at zero bias voltage. (e) Histogram of responsivity and EQE extracted from the polar diagram at 0°, 90° and 180°. (f) Histogram of detectivity and LDR extracted from the polar diagram at 0°, 90° and 180°.

photocurrent anisotropy ratio of our device is significantly superior to that of widely researched anisotropic 2D materials and their heterojunctions, such as Te, black phosphorus, WTe_2, ReS_2, $ReSe_2$, *etc.* (Fig. 5e).[6,13,14,18–21,28,29,32,54,55,64–73] This demonstrated that the as-fabricated p-Te/n-$MoSe_2$ vdWHs in this work would establish themselves as great potential building blocks for constructing polarization-sensitive photodetectors.

To further explore the polarization-sensitivity of the p-Te/n-$MoSe_2$ vdWH photodetector, responsivities of the device at 0 V with the polarized angle varying from 0 to 360° were extracted at 405 nm (24.2 mW cm^{-2}) and plotted in polar coordinates. As shown in Fig. 6a, the largest responsivity of the device could reach 314 mA W^{-1} with a high anisotropic ratio of ~16.9. In addition, polarized EQE, detectivity, and LDR are also calculated (Fig. 6b–d). The EQE could reach 96.2% with a high anisotropic ratio of ~16.39 (Fig. 6b). Importantly, a highest polarized detectivity of 1.87×10^{12} Jones could be obtained for the device, and its anisotropic ratio can reach ~14.7 (Fig. 6c). Correspondingly, the highest polarized LDR value is 102.5 dB (Fig. 6d). Compared with the reported polarization-sensitive photodetector, the excellent comprehensive performance of our device is realized (Table S1, ESI†). Fig. 6e and f show the histogram of responsivity, EQE, detectivity and LDR extracted from the polar diagram at 0°, 90° and 180°. It is obvious that our device has strong anisotropy. These results collectively demonstrate that our device possesses the ability of polarized imaging photodetection without external optical elements.

It is well known that polarization imaging with the ability to obtain polarimetric information of a scene can obtain a higher recognition rate of the target details. Until now, smart polarization imaging with small size is urgently needed for many fields including industry, medicine, and space exploration, *etc.* Therefore, to further demonstrate the polarization imaging photodetection capability of the p-Te/n-$MoSe_2$ vdWH photodetector, the device is employed as the single point-like sensing pixel in a polarization imaging system. Fig. 7a describes the schematic illustration of the polarization imaging measurement system, in which an LED screen is used to provide an unpolarized and uniform white light source. A hollow letter "SCNU" as the imaging targets is made in a black acrylic plate and placed behind the light source. The p-Te/n-$MoSe_2$ heterojunction image sensor is mounted onto a computerized 2D rotary stage, which can be moved continuously and scan the target line by line. During the image-sensing process, the photocurrent from the p-Te/n-$MoSe_2$ heterojunction photodetector was collected by a computer, and the location information for the targets is recorded simultaneously. The imaging system finally converts the input signal current into a set of gray values to form an image. The polarizer and half-wave plate are mounted in front of the focusing lens to convert the incident light irradiated on the photodetector into linearly polarized light whose polarization direction is changed by rotating the half-wave plate. Under linear polarized illumination, "SCNU" polarized imaging (365 × 180 pixels) is successfully acquired when the polarized light is at 0° and 90° (Fig. 7b and c). It should be pointed out that an obvious polarization distinction is observed, confirming the great application potential of our device.

Conclusions

In summary, after systematically investigating the noncentrosymmetric crystal structure of multilayer Te nanosheets

Published on 10 September 2021. Downloaded by Fudan University on 10/14/2021 1:32:05 PM.

 This journal is © The Royal Society of Chemistry 2021

Published on 10 September 2021. Downloaded by Fudan University on 10/14/2021 1:32:05 PM.

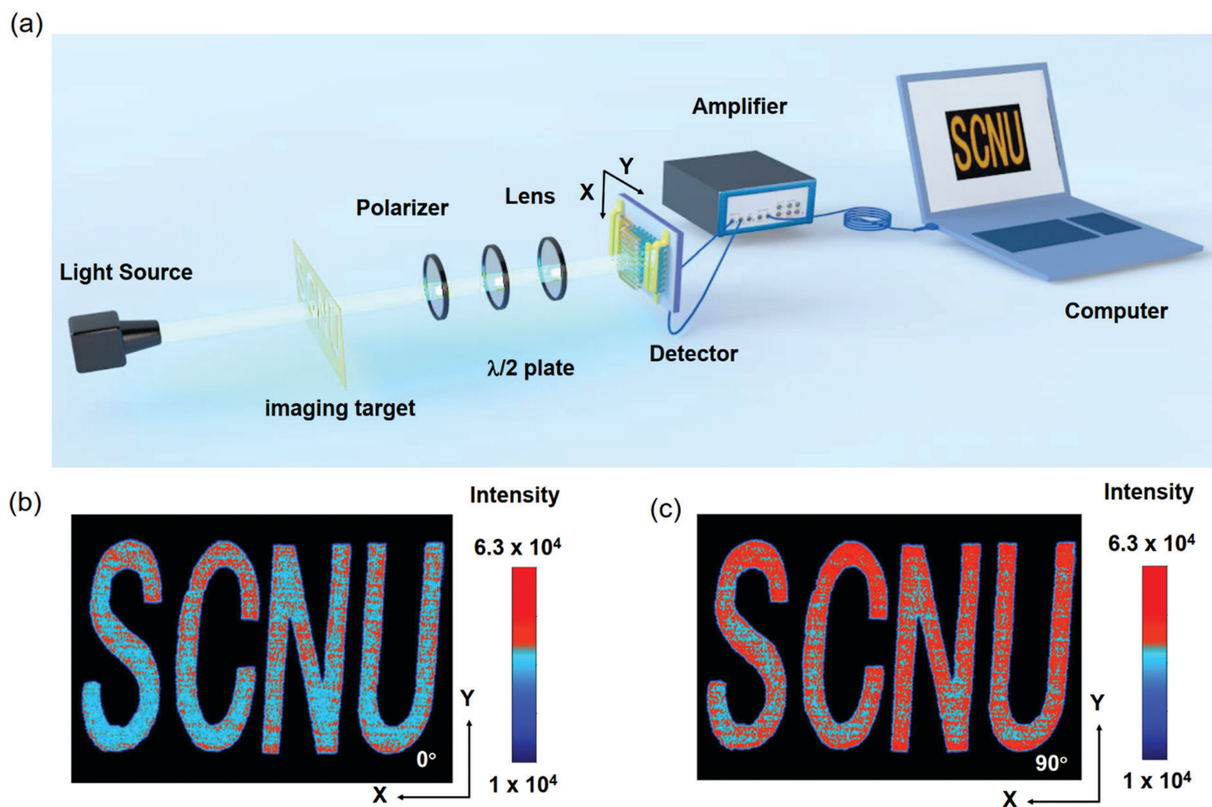

Fig. 7 Imaging sensing capability of the p-Te/n-$MoSe_2$ vdWH photodetectors. (a) Schematic diagram of the polarization imaging measurement system. (b and c) Imaging results of "SCNU" letters with polarization angles of 0° (b) and 90° (c), respectively.

by angle-resolved polarized Raman spectroscopy, a high performance polarization-sensitive imaging photodetector was fabricated based on multilayer p-Te/n-$MoSe_2$ vdWH. Such a device exhibits a large on–off ratio photocurrent (10^5), high responsivity (2106 mA W^{-1}), a fast response speed (~20 ms), and especially an ultra-high photocurrent anisotropy ratio of 16.39 at zero bias voltage. And a high detectivity (2.91×10^{13} Jones) could be obtained at a small bais voltage (−0.08 V). Thus, multilayer p-Te/n-$MoSe_2$ heterojunction devices proposed in this work were not only proposed as a potential building block for constructing a compact monolithic polarization-sensitive imaging system with low energy consumption, but also provided an additional platform for exploring novel 2D and quasi 2D materials towards practical applications.

Experimental

Device fabrication

Multilayer Te nanosheets were prepared by a solution-growth method.[31] The precursor Na_2TeO_3 and polyvinylpyrrolidone (PVP) were dissolved in deionized water to form a uniform solution under magnetic stirring, and then hydrazine hydrate (N_2H_4) and aqueous ammonia solution were added. Then the mixed solution was put into a stainless-steel autoclave lined with Teflon and the autoclave was kept at 180 °C for 20 h. After falling to room temperature, the obtained solution was centrifuged at 5000 rpm for 5 min and washed with deionized water for 3 times. $MoSe_2$ nanosheets were fabricated by the mechanical exfoliation method from bulk $MoSe_2$ crystals. The p-Te/n-$MoSe_2$ were fabricated by the target-transfer method. In this process, Te nanosheets are first transferred onto a silicon wafer covered with a 300 nm SiO_2 film by drop-casting the tellurium ethanol solution. Then, $MoSe_2$ nanosheets was exfoliated onto a transparent polydimethylsiloxane (PDMS) film by Scotch tape and aligned onto Te nanosheets *via* a three-dimensional location adjustment platform equipped with an optical microscope (Shanghai OnWay Technology Co., Ltd). The Ti/Au electrodes were patterned by the process of photoresist (ARP-5350 bought from Taizhou SUNANO New Energy Co., Ltd) spin-coated, ultraviolet exposure (*via* the markless lithography machine of TuoTuo Technology Co., Ltd.) and development to obtain the desired electrode pattern. Finally, an electron beam evaporation instrument was employed to define and deposit source/drain electrodes (5 nm Ti/60 nm Au).

Characterization

Morphologies and the contact potential difference of the samples were characterized using SEM (Hitachi S-4200) and AFM combined with KPFM (Bruker Multimode 8). The elemental composition was characterized using EDS in a Hitachi S-3400N and HT7700. The structures of Te and $MoSe_2$ nanosheets were studied by TEM (Hitachi HT7700). Raman and PL signals of the samples were collected using a micro-Raman spectrometer

System (NOST Technology, with laser excitation of 532 nm). The electrical and photoelectric properties of the photodetector were performed at room temperature using a three-probe station (Keithley Agilent B2902A system) and a multi-wavelength optical-fiber laser. Polarization imaging was measured by a polarization imaging system equipped with a camera lens (CAV-SPRATDS-V2), a 2D rotary stage (MDOM103) and an amplification circuit.

Author contributions

Qixiao Zhao, Hongyu Chen, Xiaosheng Fang and Jingbo Li conceived and designed the project. Qixiao Zhao and Feng Gao fabricated devices, and performed electrical and optoelectronic characterization of devices. Wei Gao, Mengjia Xia, Yuan Pan, Hongyan Shi, and Shichen Su contributed to the scientific discussions. The manuscript was written through the contributions of all authors. All authors have given approval to the final version of the manuscript.

Conflicts of interest

There are no conflicts to declare.

Acknowledgements

This work was supported by the National Natural Science Foundation of China (61874037), the Science and Technology Program of Guangzhou city, China (202102021121), the Pearl River Talent Recruitment Program (2019ZT08X639), and the Outstanding Young Talent Project of South China Normal University.

References

1 E. O. Polat, G. Mercier, I. Nikitskiy, E. Puma, T. Galan, S. Gupta, M. Montagut, J. J. Piqueras, M. Bouwens, T. Durduran, G. Konstantatos, S. Goossens and F. Koppens, *Sci. Adv.*, 2019, **5**, eaaw7846.
2 P. Doradla, K. Alavi, C. Joseph and R. Giles, *J. Biomed. Opt.*, 2013, **18**, 090504.
3 Y. Q. Zhao, Y. Chen, S. G. Seong and Y. Cheng, *Multi-band Polarization Imaging and Applications*, Springer, Berlin, Heidelberg, 2016.
4 W. D. Song, J. X. Chen, Z. L. Li and X. S. Fang, *Adv. Mater.*, 2021, **33**, 2101059.
5 J. Marshall and T. W. Cronin, *Curr. Biol.*, 2011, **21**, R101.
6 H. Yuan, X. Liu, F. Afshinmanesh, W. Li, G. Xu, J. Sun, B. Lian, A. G. Curto, G. Ye, Y. Hikita, Z. Shen, S. Zhang, X. Chen, M. Brongersma, H. Y. Hwang and Y. Cui, *Nat. Nanotechnol.*, 2015, **10**, 707.
7 C. J. Chen, K. K. Choi, L. Rokhinson, W. H. Chang and D. C. Tsui, *Appl. Phys. Lett.*, 1999, **74**, 862.
8 J. Wang, M. S. Gudiksen, X. Duan, Y. Cui and C. M. Lieber, *Science*, 2001, **293**, 1455.
9 A. Singh, X. Li, V. Protasenko, G. Galantai, M. Kuno, H. G. Xing and D. Jena, *Nano Lett.*, 2007, **7**, 2999.
10 Z. Fan, P. Chang, J. G. Lu, E. C. Walter, R. M. Penner, C. Lin and H. P. Lee, *Appl. Phys. Lett.*, 2004, **85**, 6128.
11 S. Hullavarad, N. Hullavarad, D. Look and B. Claflin, *Nanoscale Res. Lett.*, 2009, **4**, 1421.
12 S. Liang, B. Cheng, X. Cui and F. Miao, *Adv. Mater.*, 2020, **32**, 1903800.
13 X. Wang, Y. Li, L. Huang, X. Jiang, L. Jiang, H. Dong, Z. Wei, J. Li and W. Hu, *J. Am. Chem. Soc.*, 2017, **139**, 14976.
14 Z. Zhou, M. Long, L. Pan, X. Wang, M. Zhong, M. Blei, J. Wang, J. Fang, S. Tongay, W. Hu, J. Li and Z. Wei, *ACS Nano*, 2018, **12**, 12416.
15 Y. Yan, W. Xiong, S. Li, K. Zhao, X. Wang, J. Su, X. Song, X. Li, S. Zhang, H. Yang, X. Liu, L. Jiang, T. Zhai, C. Xia, J. Li and Z. Wei, *Adv. Opt. Mater.*, 2019, **7**, 1900622.
16 X. Wang, F. Zhong, J. Kang, C. Liu, M. Lei, L. Pan, H. Wang, F. Wang, Z. Zhou, Y. Cui, K. Liu, J. Wang, G. Shen, C. Shan, J. Li, W. Hu and Z. Wei, *Sci. China Mater.*, 2021, **64**, 1230.
17 M. Zhong, H. Meng, S. Liu, H. Yang, W. Shen, C. Hu, J. Yang, Z. Ren, B. Li, Y. Liu, J. He, Q. Xia, J. Li and Z. Wei, *ACS Nano*, 2021, **15**, 1701.
18 E. Zhang, P. Wang, Z. Li, H. Wang, C. Song, C. Huang, Z. Chen, L. Yang, K. Zhang, S. Lu, W. Wang, S. Liu, H. Fang, X. Zhou, H. Yang, J. Zou, X. Wan, P. Zhou, W. Hu and F. Xiu, *ACS Nano*, 2016, **10**, 8067.
19 F. Liu, S. Zheng, X. He, A. Chaturvedi, J. He, W. L. Chow, T. R. Mion, X. Wang, J. Zhou, Q. Fu, H. J. Fan, B. K. Tay, L. Song, R. He, C. Kloc, P. M. Ajayan and Z. Liu, *Adv. Funct. Mater.*, 2016, **26**, 1169.
20 Y. Yang, S. Liu, W. Yang, Z. Li, Y. Wang, X. Wang, S. Zhang, Y. Zhang, M. Long, G. Zhang, D. Xue, J. Hu and L. Wan, *J. Am. Chem. Soc.*, 2018, **140**, 4150.
21 P. K. Venuthurumilli, P. D. Ye and X. Xu, *ACS Nano*, 2018, **12**, 4861.
22 H. Shang, H. Chen, M. Dai, Y. Hu, F. Gao, H. Yang, B. Xu, S. Zhang, B. Tan, X. Zhang and P. Hu, *Nanoscale Horiz.*, 2020, **5**, 564.
23 J. He, H. Chen, Q. Zhao, Y. Wang, Y. Pan, S. Huang, F. C. Ling, S. Wang and S. Su, *J. Mater. Chem. C*, 2021, **9**, 9484–9491.
24 Y. Wang, L. Li, H. Wang, L. Su, H. Chen, W. Bian, J. Ma, B. Li, Z. Liu and A. Shen, *Nanoscale*, 2020, **12**, 1406.
25 M. Dai, H. Chen, R. Feng, W. Feng, Y. Hu, H. Yang, G. Liu, X. Chen, J. Zhang, C. Xu and P. Hu, *ACS Nano*, 2018, **12**, 8739.
26 L. Han, M. Yang, P. Wen, W. Gao, N. Huo and J. Li, *Nanoscale Adv.*, 2021, **3**, 2657.
27 M. Hussain, S. H. A. Jaffery, A. Ali, C. D. Nguyen, S. Aftab, M. Riaz, S. Abbas, S. Hussain, Y. Seo and J. Jung, *Sci. Rep.*, 2021, **11**, 3688.
28 Y. Xin, X. Wang, Z. Chen, D. Weller, Y. Wang, L. Shi, X. Ma, C. Ding, W. Li, S. Guo and R. Liu, *ACS Appl. Mater. Interfaces*, 2020, **12**, 15406.
29 S. Zhao, J. Wu, K. Jin, H. Ding, T. Li, C. Wu, N. Pan and X. Wang, *Adv. Funct. Mater.*, 2018, **28**, 1802011.

Published on 10 September 2021. Downloaded by Fudan University on 10/14/2021 1:32:05 PM.

This journal is © The Royal Society of Chemistry 2021

Published on 10 September 2021. Downloaded by Fudan University on 10/14/2021 1:32:05 PM.

30 L. Zeng, S. Lin, Z. Li, Z. Zhang, T. Zhang, C. Xie, C. Mak, Y. Chai, S. P. Lau, L. Luo and Y. H. Tsang, *Adv. Funct. Mater.*, 2018, **28**, 1705970.
31 Y. Wang, G. Qiu, R. Wang, S. Huang, Q. Wang, Y. Liu, Y. Du, W. A. Goddard, M. J. Kim, X. Xu, P. D. Ye and W. Wu, *Nat. Electron.*, 2018, **1**, 228.
32 M. Amani, C. Tan, G. Zhang, C. Zhao, J. Bullock, X. Song, H. Kim, V. R. Shrestha, Y. Gao, K. B. Crozier, M. Scott and A. Javey, *ACS Nano*, 2018, **12**, 7253.
33 M. Bernardi, M. Palummo and J. C. Grossman, *Nano Lett.*, 2013, **13**, 3664.
34 X. Chen, H. Yang, G. Liu, F. Gao, M. Dai, Y. Hu, H. Chen, W. Cao, P. Hu and W. Hu, *Adv. Funct. Mater.*, 2018, **28**, 1705153.
35 A. B. Patel, P. Chauhan, K. Patel, C. K. Sumesh, S. Narayan, K. D. Patel, G. K. Solanki, V. M. Pathak, P. K. Jha and V. Patel, *ACS Sustainable Chem. Eng.*, 2020, **8**, 4809.
36 L. Tong, X. Huang, P. Wang, L. Ye, M. Peng, L. An, Q. Sun, Y. Zhang, G. Yang, Z. Li, F. Zhong, F. Wang, Y. Wang, M. Motlag, W. Wu, G. J. Cheng and W. Hu, *Nat. Commun.*, 2020, **11**, 2308.
37 M. Hirayama, R. Okugawa, S. Ishibashi, S. Murakami and T. Miyake, *Phys. Rev. Lett.*, 2015, **114**, 206401.
38 Y. Du, G. Qiu, Y. Wang, M. Si, X. Xu, W. Wu and P. D. Ye, *Nano Lett.*, 2017, **17**, 3965.
39 D. Wines, J. A. Kropp, G. Chaney, F. Ersan and C. Ataca, *Phys. Chem. Chem. Phys.*, 2020, **22**, 6727.
40 G. Dresselhaus and A. S. Pine, *Phys. Rev. B: Solid State*, 1971, **4**, 356.
41 P. Nagler, G. Plechinger, C. Schüler and T. Korn, *Phys. Status Solidi RRL*, 2016, **10**, 185.
42 G. Lucovsky, K. Helliwell and R. M. Martin, *Phys. Rev. B: Solid State*, 1976, **13**, 1383.
43 P. Y. Yu, M. Cardona, P. Y. Yu and M. Cardona, *Fundamentals of Semiconductors—Physics and Material Properties*, 3rd edn, Springer, Berlin, 2001.
44 Y. Deng, Z. Luo, N. J. Conrad, H. Liu, Y. Gong, S. Najmaei, P. M. Ajayan, J. Lou, X. Xu and P. D. Ye, *ACS Nano*, 2014, **8**, 8292.
45 C. Sah, R. N. Noyce and W. Shockley, *Proc. IRE*, 1957, **45**, 1228.
46 J. Tao, J. Jiang, S. Zhao, Y. Zhang, X. Li, X. Fang, P. Wang, W. Hu, Y. H. Lee, H. Lu and D. Zhang, *ACS Nano*, 2021, **15**, 3241.
47 C. K. Zankat, P. M. Pataniya, A. Patel, S. A. Bhakhar, S. Narayan, G. K. Solanki, K. D. Patel, V. M. Pathak, C. K. Sumesh and P. K. Jha, *Mater. Today Energy*, 2020, **18**, 100550.
48 C. Bao, Z. Chen, Y. Fang, H. Wei, Y. Deng, X. Xiao, L. Li and J. Huang, *Adv. Mater.*, 2017, **29**, 1703209.
49 J. B. Barton, R. F. Cannata and S. M. Petronio, *Pro. SPIE*, 2002, **4721**, 37.
50 X. Gong, M. Tong, Y. Xia, W. Cai, J. S. Moon, Y. Cao, G. Yu, C. L. Shieh, B. Nilsson and A. J. Heeger, *Science*, 2009, **325**, 1665.
51 A. A. M. El-Amir, T. Ohsawa, S. Ishii, M. Imura, H. Segawa, I. Sakaguchi, T. Nagao, K. Shimamura and N. Ohashi, *AIP Adv.*, 2019, **9**, 055024.
52 F. Ahmed, Y. D. Kim, Z. Yang, P. He, E. Hwang, H. Yang, J. Hone and W. J. Yoo, *Nat. Commun.*, 2018, **9**, 3414.
53 J. Mao, Y. Yu, L. Wang, X. Zhang, Y. Wang, Z. Shao and J. Jie, *Adv. Sci.*, 2016, **3**, 1600018.
54 L. Tong, X. Duan, L. Song, T. Liu, L. Ye, X. Huang, P. Wang, Y. Sun, X. He, L. Zhang, K. Xu, W. Hu, J. Xu, J. Zang and G. J. Cheng, *Appl. Mater. Today*, 2019, **15**, 203.
55 C. Jia, D. Wu, E. Wu, J. Guo, Z. Zhao, Z. Shi, T. Xu, X. Huang, Y. Tian and X. Li, *J. Mater. Chem. C*, 2019, **7**, 3817.
56 F. Yan, L. Zhao, A. Patan, P. Hu, X. Wei, W. Luo, D. Zhang, Q. Lv, Q. Feng, C. Shen, K. Chang, L. Eaves and K. Wang, *Nanotechnology*, 2017, **28**, 27LT01.
57 Q. Lv, F. Yan, X. Wei and K. Wang, *Adv. Opt. Mater.*, 2018, **6**, 1700490.
58 F. Qin, F. Gao, M. Dai, Y. Hu, M. Yu, L. Wang, W. Feng, B. Li and P. Hu, *ACS Appl. Mater. Interfaces*, 2020, **12**, 37313.
59 Y. Liu, C. Zhao, J. Li, S. Zhao, X. Xu, H. Y. Fu, C. Yu, F. Kang and G. Wei, *ACS Appl. Electron. Mater.*, 2021, **3**, 1236.
60 N. Wazir, R. Liu, C. Ding, X. Wang, X. Ye, X. Lingling, T. Lu, L. Wei and B. Zou, *ACS Appl. Nano Mater.*, 2020, **3**, 7543.
61 C. K. Zankat, P. M. Pataniya, A. Patel, S. A. Bhakhar, S. Narayan, G. K. Solanki, K. D. Patel, V. M. Pathak, C. K. Sumesh and P. K. Jha, *Mater. Today Energy*, 2020, **18**, 100550.
62 W. Gao, F. Zhang, Z. Zheng and J. Li, *ACS Appl. Mater. Interfaces*, 2019, **11**, 19277.
63 B. Liu, J. Du, H. Yu, M. Hong, Z. Kang, Z. Zhang and Y. Zhang, *Nano Res.*, 2021, **14**, 1734.
64 L. Pi, C. Hu, W. Shen, L. Li, P. Luo, X. Hu, P. Chen, D. Li, Z. Li, X. Zhou and T. Zhai, *Adv. Funct. Mater.*, 2020, **31**, 2006774.
65 L. Li, P. Gong, D. Sheng, S. Wang, W. Wang, X. Zhu, X. Shi, F. Wang, W. Han, S. Yang, K. Liu, H. Li and T. Zhai, *Adv. Mater.*, 2018, **30**, 1804541.
66 W. Zhou, J. Chen, H. Gao, T. Hu, S. Ruan, A. Stroppa and W. Ren, *Adv. Mater.*, 2019, **31**, 1804629.
67 N. Zuo, A. Nie, C. Hu, W. Shen, B. Jin, X. Hu, Z. Liu, X. Zhou and T. Zhai, *Small*, 2021, **17**, 2008078.
68 J. Qiao, F. Feng, Z. Wang, M. Shen, G. Zhang, X. Yuan and M. G. Somekh, *ACS Appl. Mater. Interfaces*, 2021, **13**, 17948.
69 Y. Cui, Z. Zhou, X. Wang, X. Wang, Z. Ren, L. Pan and J. Yang, *Nano Res.*, 2021, **14**, 2224.
70 S. Zhao, P. Luo, S. Yang, X. Zhou, Z. Wang, C. Li, S. Wang, T. Zhai and X. Tao, *Adv. Opt. Mater.*, 2021, **9**, 2100198.
71 D. Kim, K. Park, J. H. Lee, I. S. Kwon, I. H. Kwak and J. Park, *Small*, 2021, **17**, 2006310.
72 J. Lai, X. Liu, J. Ma, Q. Wang, K. Zhang, X. Ren, Y. Liu, Q. Gu, X. Zhuo, W. Lu, Y. Wu, Y. Li, J. Feng, S. Zhou, J. Chen and D. Sun, *Adv. Mater.*, 2018, **30**, 1707152.
73 L. Ye, P. Wang, W. Luo, F. Gong, L. Liao, T. Liu, L. Tong, J. Zang, J. Xu and W. Hu, *Nano Energy*, 2017, **37**, 53.